Hygroscopic Properties of CH_3SO_3Na, $CH_3SO_3NH_4$, $(CH_3SO_3)_2Mg$, and $(CH_3SO_3)_2Ca$ Particles Studied by micro-FTIR Spectroscopy

Yong Liu and Alexander Laskin*

William R. Wiley Environmental Molecular Sciences Laboratory, Pacific Northwest National Laboratory, P.O. Box 999, MSIN K8-88, Richland, Washington 99352

Received: September 5, 2008; Revised Manuscript Received: December 1, 2008

The hygroscopic behavior of CH_3SO_3Na, $CH_3SO_3NH_4$, $(CH_3SO_3)_2Mg$, and $(CH_3SO_3)_2Ca$ particles as a function of relative humidity (RH) has been studied using microscopic Fourier transform infrared (micro-FTIR) spectroscopy. The approach used exposure of substrate-deposited, ~1 μm dry-size particles to humidified nitrogen followed by micro-FTIR spectroscopy over a selected sample area. The results show that CH_3SO_3Na particles undergo characteristic phase transitions at deliquescence relative humidity (DRH) of 71% and efflorescence relative humidity (ERH) of ~40%. In contrast, $CH_3SO_3NH_4$, $(CH_3SO_3)_2Mg$, and $(CH_3SO_3)_2Ca$ particles do not undergo phase transitions and exhibit continuous, reversible uptake and evaporation of water under the influence of changing RH. The extent of water uptake is quantified and presented as water-to-solute ratios (WSR) in particles as a function of RH. The WSR values are determined from the integrated absorbance of the water and the solute-specific bands in IR spectra recorded at different RH.

Introduction

Atmospheric aerosols play an important role in environmental issues related to air quality and climate change. Aerosols influence Earth's climate directly and indirectly via scattering and absorption of solar radiation, formation of clouds, and precipitation.[1,2] They provide surfaces for heterogeneous reactions, hence affecting atmospheric composition and chemistry.[3] It is well-known that the extent to which aerosol particles impact chemistry and radiative balance of the atmosphere depends on their size, phase, chemical composition, and water content, all of which are highly dependent on relative humidity (RH) and hygroscopic properties of corresponding particles.[4,5] For example, heterogeneous reactions of nitric acid with sea salt[6,7] and mineral dust[8,9] particles are considerably faster under those RH conditions where original and/or reaction-modified particles exist in aqueous phase. Likewise, scattering cross sections of deliquesced and hygroscopically grown particles at high RH are much greater than those of crystalline, solid particles at the RH below the efflorescence point.[10,11] Therefore, a quantitative understanding of hygroscopic properties of particles as a function of RH is critical toward understanding their impacts on atmospheric environment.

Over the last few decades, phase and hygroscopic properties of environmental particles of atmospheric relevance have been reported in many experimental and modeling studies (e.g., refs 12−15 and citations therein). Specifically, much attention has been given to the hygroscopic and optical properties of particles composed of sea salt and mineral dust as well as those internally mixed with nitrates and sulfates resulting from their chemical processing in the atmosphere.

Over the oceans, sea salt and mineral dust particles can also be processed by methanesulfonic acid (CH_3SO_3H, MSA), an important oxidation product of dimethyl sulfide (CH_3SCH_3, DMS). Biogenic emissions of DMS from marine phytoplankton account for approximately 60% of the total natural sulfur gases released to the atmosphere[16] and have been reported to have substantial impact on radiative forcing as a result of formation of sulfate aerosols.[17] For many years, conversion of DMS to particulate sulfate aerosols was assumed to be a dominant reaction pathway for DMS in the marine boundary layer (MBL). However, recent modeling[18] and field[19] studies indicate that under certain condition DMS does not preferentially convert to sulfate, but rather ends up in particles as methanesulfonate salts, which previously have been considered only of minor importance. These findings indicate that modeling of the MBL aerosols and cloud formation processes require extensive data on the hygroscopic properties of relevant methanesulfonate salts, which are currently scarce. To the best of our knowledge, there is only one set of the literature data reported for CH_3SO_3Na particles.[20]

In this paper, Fourier transform infrared microspectroscopy (micro-FTIR) is used to investigate the hygroscopic properties of ~1 μm dry-size, substrate-deposited particles of four atmospherically relevant methanesulfonate salts: CH_3SO_3Na, $CH_3SO_3NH_4$, $(CH_3SO_3)_2Mg$ and $(CH_3SO_3)_2Ca$. We use changes in the micro-FTIR acquired spectra to determine deliquescence relative humidity (DRH), efflorescence relative humidity (ERH), and water-to-solute molar ratios characteristic for each type of the particles.[21] Supplementary measurements using attenuated total reflection FTIR spectroscopy were performed to determine cross section of a methanesulfonate-specific absorption band ($\nu_8(-SO_3^-)$ asymmetric stretch) characteristic for studied salts. We report that CH_3SO_3Na particles exhibit distinct phase transitions at 71% DRH and ~49% ERH, in a good agreement with previously reported studies.[20] In contrast, $CH_3SO_3NH_4$, $(CH_3SO_3)_2Mg$, and $(CH_3SO_3)_2Ca$ undergo continuous hygroscopic changes without hysteresis between hydration and dehydration cycles.

Experimental Section

Aerosols of CH_3SO_3Na, $CH_3SO_3NH_4$, $(CH_3SO_3)_2Mg$, and $(CH_3SO_3)_2Ca$ were atomized from aqueous 0.5 M solutions

* To whom correspondence should be addressed. E-mail: Alexander.Laskin@pnl.gov. Phone: 1-509-371-6129. Fax: 1-509-371-6139.

10.1021/jp8079149 CCC: $40.75
Published on Web 01/26/2009

prepared from corresponding salts. CH_3SO_3Na (98.0% purity) and $CH_3SO_3NH_4$ (98.0% purity) purchased from Aldrich, Inc. were used without additional purification. As $(CH_3SO_3)_2Mg$ and $(CH_3SO_3)_2Ca$ are not commercially available, we prepared samples of these salts by mixing CH_3SO_3H and $MgCl_2$, ($CaCl_2$) in aqueous solutions with a ratio of $CH_3SO_3^-$-to-Mg^{2+} (Ca^{2+}) slightly higher than two to ensure complete displacement of chlorine as a result of an acid ion-exchange reaction of

$$MgCl_2(aq)/CaCl_2(aq) + 2CH_3SO_3H(aq) \rightarrow (CH_3SO_3)_2Mg(aq)/(CH_3SO_3)_2Ca(aq) + 2HCl(g) \quad (R1)$$

A beaker with the corresponding solution was placed in an oven at 100 °C, followed by overnight treatment in vacuum to release HCl and excessive CH_3SO_3H. The obtained powders of $(CH_3SO_3)_2Mg$ and $(CH_3SO_3)_2Ca$ were used to generate aerosols. The generated aerosol particles were dried in a diffusion drier (TSI, Inc., model 3062) prior to sizing and substrate deposition with a micro-orifice uniform deposition impactor (MOUDI) (MSP, Inc., model 110). In this study, we used stage 5 of the MOUDI with an aerodynamic cutoff size of 1 μm for particle collection. The particles were deposited on transmission electron microscopy (TEM) grids (carbon type-B, 400 mesh nickel grids, Ted Pella, Inc.) mounted on the impaction plate. Similar to previous studies[6,8,21] narrow size distributions of deposited particles were confirmed by computer-controlled scanning electron microscopy (CCSEM). The number size distributions of deposited particles were log−normal with median diameters $\bar{D} = 0.78$ μm for CH_3SO_3Na, 1.15 μm for $CH_3SO_3NH_4$, 1.24 μm for $(CH_3SO_3)_2Mg$, and 1.19 μm for $(CH_3SO_3)_2Ca$ based on the CCSEM measurements of equivalent circle diameters of projected areas of particles in microscopy images. The geometric standard deviations fall within the range of $\sigma = 1.2-1.8$. The total particle densities were approximately $(3-6) \times 10^6$ particles/cm^2 of the substrate. Elemental analysis of particles in the prepared samples was done using CCSEM with energy-dispersed analysis of X-rays (EDX). The results indicated that the Cl signal was indistinguishable from background in the samples of $(CH_3SO_3)_2Mg$ and $(CH_3SO_3)_2Ca$ particles.

Detailed description of the micro-FTIR experimental setup and its application for studies of particle phase transitions and hygroscopic growth has been reported elsewhere.[21] In brief, the apparatus comprised a Bruker A590 IR optical microscope interfaced with a Bruker IFS 66/S FTIR spectrometer equipped with a liquid-nitrogen-cooled mercury−cadmium−telluride (MCT) detector. Turning mirrors were used to switch between pathways for visible (optical mode) and IR irradiation of the sample. Cassegrainian optics was used to focus the IR beam on the sample and to collect the transmitted IR light after its interaction with the sample. The TEM grid substrate with deposited particles was placed in a sandwich-like sample holder, which was tightly affixed to the surface of temperature-controlled silver block using a standard spring-loaded insert in a sealable environmental stage (model THMS 600, Linkam, Inc.). An aperture placed in the optical path defined the sample area over which the IR spectrum was collected. The RH over the particle sample was controlled by a continuous flow of a mixture of dry and humidified nitrogen provided by a model LI-610 dew point generator (LI-COR, Inc.) with a total flow rate of ~1.0 slpm. A dew point hygrometer (model HMP234, Vaisala, Inc.) was used to monitor RH of the combined flows with an accuracy of ±1%. All experiments were performed with particle samples kept at $T = 24$ °C.

Micro-FTIR experiments were performed as follows. First, the microscope was set in the optical mode, which allows only the specific circular area of the sample defined by the aperture to be probed. After switching the microscope to the IR transmission mode, FTIR absorbance spectra were acquired by coadding 512 scans at a resolution of 4 cm^{-1}. A background spectrum with the same scan number was collected on a blank TEM grid without particles. After changing RH to a new setting, a typical delay of ~5 min was required before equilibrium between particles and water had been reached. Time required to reach equilibrium was elucidated in series of experiments where a number of consecutive IR spectra were acquired immediately after the new RH value was set. The IR spectra collected after 5 min delay showed reproducible overlap between consecutive spectra, indicating effective equilibrium in the system. An ensemble of approximately 80−100 particles was monitored in each of the experiments, which corresponds to ~1 pmol of the solute material being probed. Condensed-phase water in the particles was quantified from the integrated absorbance of the OH stretching band.

To determine water-to-solute molar ratios in the particles composed of methanesulfonate salts, cross section of some prominent IR absorption band characteristic for the studied salts is needed. In the present work, attenuated total reflection (ATR) FTIR experiments were carried out for measurements of the integrated cross section of methanesulfonate-specific SO_3 absorption band (ν_8, SO_3 asym stretch) in the particle samples. A Bruker IFS 66/S FTIR spectrometer equipped with a liquid-nitrogen-cooled detector, a KBr beam splitter, and an attenuated total reflectance accessory with 45° ZnSe reflection crystal was used to collect the IR spectra. CH_3SO_3Na solutions with known concentrations were added to cover the surface of the crystal. For each given concentration, sample spectra were acquired by averaging 512 scans at a resolution of 4 cm^{-1}, and a background ZnSe crystal spectrum was collected with the same number of scans. Integrated absorbances of $\delta(H_2O)$ and $\nu_8(-SO_3^-)$ vibration modes were used to quantify the integrated cross section of the $\nu_8(-SO_3^-)$ band as will be described below. Acquisition of few consecutive spectra over the same sample solution revealed nearly identical spectra that indicate negligible concentration changes that possibly could result from water evaporation during the time of experiment.

Results and Discussion

Figure 1 shows representative SEM images of CH_3SO_3Na, $CH_3SO_3NH_4$, $(CH_3SO_3)_2Mg$, and $(CH_3SO_3)_2Ca$ particles deposited on TEM grids and used in this study. The micro-FTIR probed area, defined by the aperture, was 1×10^{-9} m^2 in our experiments, which is approximately 10-fold larger than the single field-of-view of the presented SEM images. As can be inferred from the microscopy images, the CH_3SO_3Na particles resemble morphologies with clear contour and are likely exhibit crystalline phase of particles. In contrast, $CH_3SO_3NH_4$, $(CH_3SO_3)_2Mg$, and $(CH_3SO_3)_2Ca$ particles indicate more droplet-like morphologies, implying their likely metastable, amorphous solid-phase form. Accordingly, the two-dimensional (2-D) projection areas of $CH_3SO_3NH_4$, $(CH_3SO_3)_2Mg$, and $(CH_3SO_3)_2Ca$ particles appear to be larger than that of CH_3SO_3Na. This observation falls in with the presumption that when these amorphous, perhaps jelly-like, particles are impacted onto the substrate, the impaction flattens them against the substrate, resulting in 2-D projection areas larger than their original airborne size. As will be discussed below, the amorphous form of these particles is also consistent with the data presented in the next sections of this manuscripts as well as

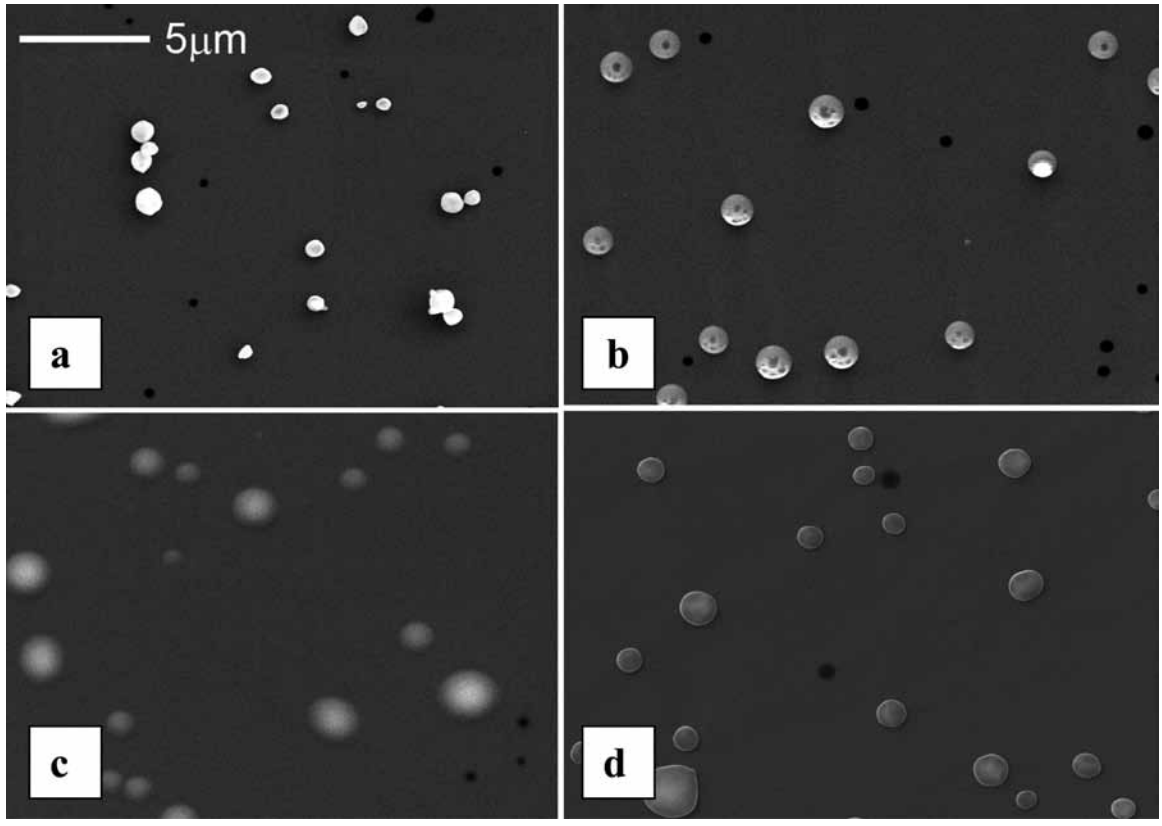

Figure 1. SEM images of (a) CH_3SO_3Na, (b) $CH_3SO_3NH_4$, (c) $(CH_3SO_3)_2Mg$, and (d) $(CH_3SO_3)_2Ca$ particle samples. Depicted size bar on panel a is common for all four images.

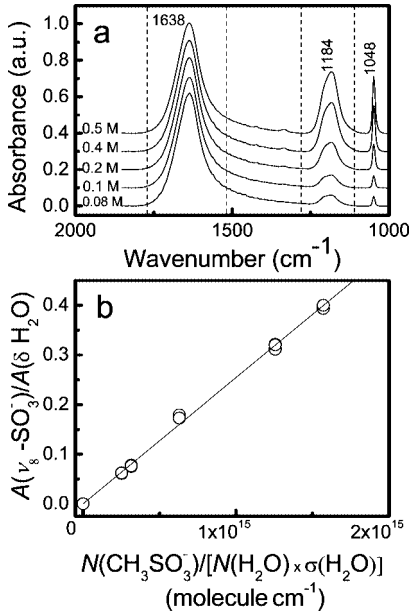

Figure 2. (a) ATR-IR spectra of CH_3SO_3Na solutions with varying concentration. (b) A plot on the basis of the Beer−Lambert law used for calculation of the integrated (1110−1280 cm^{-1}) cross section of a $\nu_8(-SO_3^-)$ band.

with our previous observations of amorphous $NaNO_3$ and $Ca(NO_3)_2$ particles.[21,22]

Figure 2a shows the ATR-FTIR spectra of CH_3SO_3Na solutions with different concentration ranging from 0.08 to 0.5 M. The spectra have a strong absorption band at 1638 cm^{-1} due to the $\delta(H_2O)$ bending mode and two bands centered at 1184 and 1048 cm^{-1}, which are assigned to $\nu_8(-SO_3^-)$ asymmetric and $\nu_3(-SO_3^-)$ symmetric stretching modes in the $CH_3SO_3^-$ ions, respectively.[23] As seen, absorption of the $\nu_8(-SO_3^-)$ and $\nu_3(-SO_3^-)$ stretching modes increase as the concentration of $CH_3SO_3^-$ is raised while absorption of the $\delta(H_2O)$ bending mode remains nearly the same for all the solutions. Integrated absorbances of the $\delta(H_2O)$ mode in the region from 1770 to 1520 cm^{-1} and the $\nu_8(-SO_3^-)$ mode in the region from 1280 to 1110 cm^{-1} were used to obtain the integrated cross section of the $\nu_8(-SO_3^-)$ band using the following equation on the basis of the Beer−Lambert law:

$$\bar{\sigma}_{\nu_8(-SO_3^-)} = \bar{\sigma}_{\delta(H_2O)} \frac{(N_{H_2O})(\bar{A}_{\nu_8(-SO_3^-)})}{(N_{CH_3SO_3^-})(\bar{A}_{\delta(H_2O)})} \quad (1)$$

where $\bar{\sigma}_{\nu_8(-SO_3^-)} = \int_{1110}^{1280} \sigma_{\nu_8(-SO_3^-)}\, d\nu$ denotes the integrated cross section of $\nu_8(-SO_3^-)$ band; $\bar{\sigma}_{\delta(H_2O)} = \int_{1520}^{1770} \sigma_{\delta(H_2O)}\, d\nu$ is the integrated cross section of the $\delta(H_2O)$ bending mode reported for bulk water as 5.73×10^{-18} cm·molecule^{-1},[24] and N_{H_2O} and $N_{CH_3SO_3^-}$ are numbers of water molecules and $CH_3SO_3^-$ ions in the solutions; $\bar{A}_{\delta(H_2O)} = \int_{1520}^{1770} A_{H_2O}\, d\nu$ and $\bar{A}_{\nu_8(-SO_3^-)} = \int_{1110}^{1280} A_{\nu_8(-SO_3^-)}\, d\nu$ are the integrated absorbances of the $\delta(H_2O)$ bending and the $\nu_8(-SO_3^-)$ asymmetric stretching bands.

The value of $\bar{\sigma}_{\nu_8(-SO_3^-)}$ may be determined from the slope of a linear fit of the $\bar{A}_{\nu_8(-SO_3^-)}/\bar{A}_{\delta(H_2O)}$ ratio versus $N_{CH_3SO_3^-}/(N_{H_2O}\bar{\sigma}_{\delta(H_2O)})$ experimental data as plotted in Figure 2b. The fit yields a value of $\bar{\sigma}_{\nu_8(-SO_3^-)} = (2.54 \pm 0.38) \times 10^{-16}$ cm·molecule^{-1}. As no literature value has been reported previously, to have additional confidence in our ATR-FTIR experiment, we applied the same approach to measure the integrated cross section of a $\nu_3(NO_3^-)$ asymmetric stretching band in nitrate salts, which has been well documented in the literature. In our experiment, the corresponding integrated cross section was found to be $\bar{\sigma}_{\nu_3(NO_3^-)} = 2.5 \times 10^{-16}$ cm·molecule^{-1}, in good agreement with previously reported values by Al-Abadleh and Grassian[25] (2.4×10^{-16} cm·molecule^{-1}) and

Sporleder and Ewing[26] (3.0×10^{-16} cm·molecule^{-1}). It should be noted that in the present work the $\bar{\sigma}_{\nu_8(-SO_3^-)}$ integrated cross section obtained from the ATR-FTIR measurements in bulk solutions is used for quantification of amount of methanesulfonate solutes even though that absorption band position and its shape in the concentrated (supersaturated) and solid-phase particles are somewhat different from those corresponding to the bulk solution of the same compound. Nevertheless, as shown in previous study[26] the integrated cross sections in supersaturated and even solid phases agree reasonably well with those in aqueous phase, and it is feasible to use their values for the calculation of water-to-solute ratios (WSR) in particle hydration studies.[21]

To investigate water cycles and hygroscopic properties characteristic for particles selected in this work, we inferred the WSR from corresponding IR spectra by integrating the areas of H_2O and SO_3 absorption bands using the following equation:

$$\mathrm{WSR} = \frac{N_{H_2O}}{N_{(CH_3SO_3)_nX}} = \frac{N_{H_2O}}{nN_{CH_3SO_3^-}} = \frac{(\bar{\sigma}_{\nu_8(-SO_3^-)})(\bar{A}_{\nu(H_2O)})}{(\bar{\sigma}_{\nu(H_2O)})(\bar{A}_{\nu_8(-SO_3^-)})} \quad (2)$$

where $(CH_3SO_3)_nX$ depicts chemical formula of the methanesulfonate salts, $\bar{A}_{\nu(H_2O)}$ is the integrated absorbance of the $\nu(H_2O)$ stretching band (cm^{-1}), and $\bar{A}_{\nu_8(-SO_3^-)}$ is the integrated absorbance of the $\nu_8(-SO_3^-)$ asymmetric stretching band (cm^{-1}). The integrated absorbance of the $\nu(H_2O)$ band in the region from 3660 to 2750 cm^{-1} is used to quantify the amount of water in particles using the corresponding cross section of $\bar{\sigma}_{\nu(H_2O)} = 1.07 \times 10^{-16}$ cm·molecule^{-1} reported for bulk water.[27] The integrated absorbance of the $\nu_8(-SO_3^-)$ band in the region from 1280 to 1110 cm^{-1} is used to quantify the amount of $CH_3SO_3^-$ solute ions in particles. In our previous work,[21] we have reported that ~1 pmol of solute material is typically sufficient for reliable measurements of the WSR values in hydrating/dehydrating particles. Specifically, pilot studies[21] with NaCl, $NaNO_3$, and $(NH_4)_2SO_4$ particles, as well as study with CH_3SO_3Na particles presented in this manuscript, have shown WSR values within 10−15% of the data margin reported in traditional levitation experiments.

Figure 3a shows IR spectra acquired for an ensemble of CH_3SO_3Na particles over a sample area at increasing RH. As can be seen, no appreciable water absorbance is seen in the region of 3660−2750 cm^{-1} at RH below 70%. Detailed IR spectra for the region of 1000−1400 cm^{-1} wavenumbers and assignments of the specific vibration modes are presented in Figure 4 and Table 1. The corresponding spectra consists of a prominent doublet of $\nu_8(-SO_3^-)$ bands centered at 1197 and 1209 cm^{-1} along with an additional satellite at 1248 cm^{-1}, which are all indicative of the crystalline phase of CH_3SO_3Na particles.[28] The splitting of this degenerate mode is due to a loss of symmetry in the crystal compared to the free ion.[29−32] A similar phenomenon has been observed in crystalline nitrate particles.[15,21,33] A group of less intensive absorption bands around 1062 cm^{-1} is assigned to a $\nu_3(-SO_3^-)$ symmetric stretching mode. The narrow, structured bands at low RH have been commonly observed in the crystalline aerosols.[21]

As the RH was incrementally raised, absorption spectra were continuously recorded (spectra from 0% to 60% RH not shown here). Condensed-phase water remains undetectable until RH approaches 70−71%, where absorption of the $\delta(H_2O)$ band becomes first evident and then rapidly expands at RH higher than 71%. Therefore, it appears that CH_3SO_3Na particles deliquesce at ~71% DRH, resulting in an abrupt increase in the absorbance of around ~3400 cm^{-1} and a spontaneous transformation from solid CH_3SO_3Na particles to saturated solution droplets. Simultaneously, the group of $\nu_8(-SO_3^-)$ narrow bands broadens significantly forming one peak shifted to 1192 cm^{-1}. Likewise, the 1062 cm^{-1} peak indicates red shift to 1049 cm^{-1}. The observed less structured, broad bands are characteristic of deliquesced particles, and the band shape and position changes are consistent with observations of particles undergoing deliquescence phase transition. The positions and shapes of the $\nu_8(-SO_3^-)$ and $\nu_3(-SO_3^-)$ bands at 71% resemble those observed in bulk solution in the ATR-IR experiments shown in Figure 2. Above 71% RH, the CH_3SO_3Na deliquesced particles continue to grow with further increases in RH as indicated by growth and expansion of the $\delta(H_2O)$ band.

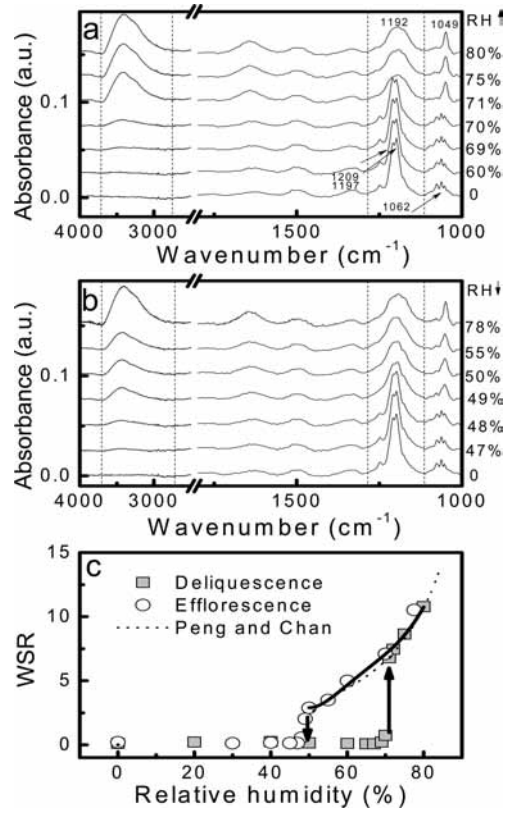

Figure 3. IR spectra of CH_3SO_3Na particles undergoing (a) hydration and (b) dehydration (top panels). Spectra are vertically offset for clarity. (c) Variations of WSRs in CH_3SO_3Na particles during hydration and dehydration experiments. Data from Peng and Chan (ref 20) (dashed line) are also included for comparison. Solid line is a polynomial fit of the experimental data (Table 2).

IR spectra of the CH_3SO_3Na particles recorded in the dehydration cycle are shown in Figure 3b. Their variations are merely in the reversed order. Upon decreasing RH, the deliquesced CH_3SO_3Na particles gradually lose their water content and water bands in the FTIR spectra shrink gradually until an abrupt shrinkage in absorbance occurs at about 49% ERH where particle effloresce and become crystalline again.

Figure 3c shows a complete hydration/dehydration cycle of CH_3SO_3Na particles recorded in the micro-FTIR experiment. Here, the change of particle water content is expressed as the WSR values plotted as a function of RH. Evidently, CH_3SO_3Na particles show nearly no water content before they deliquesce and start to grow hygroscopically. Upon evaporation, the particles slowly shed their water content prior the efflorescence phase transition. The hysteresis observed in the water cycle of the CH_3SO_3Na particles is very typical for inorganic salts. A

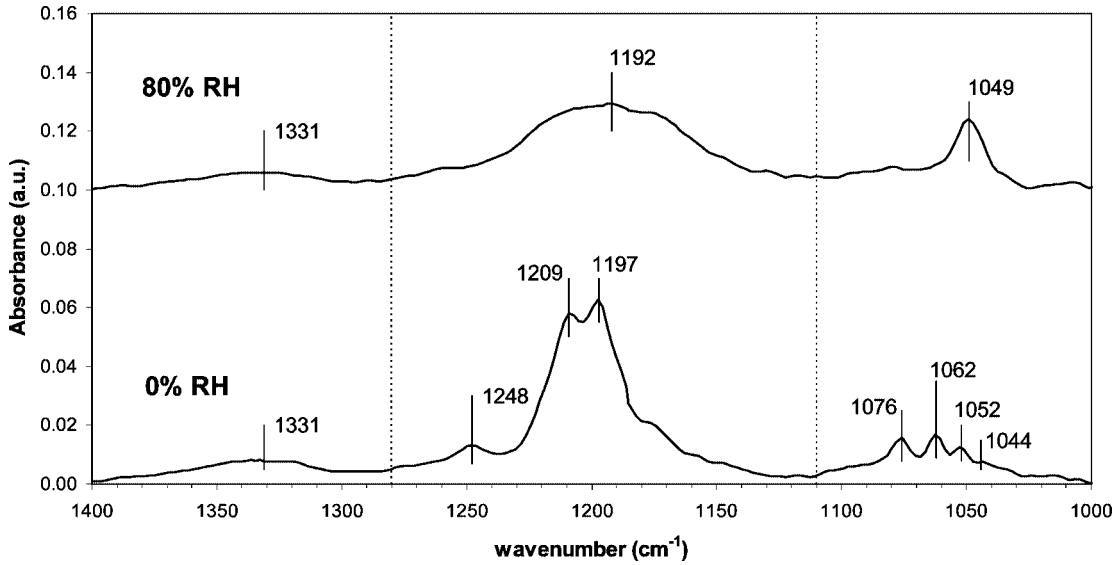

Figure 4. Fragments (1000−1400 cm^{-1} region) of the experimental FTIR spectra of CH_3SO_3Na particles recorded in the hydration experiment at 0% and 80% RH.

TABLE 1: IR Vibrational Frequencies (cm^{-1}) of the Normal Modes for Solid-State CH_3SO_3Na and Aqueous $CH_3SO_3^-$ Ions Observed in This Work and Reported in Literature within the Range of 1000−1400 cm^{-1}

CH_3SO_3Na particles at 0% RH (this work)[a]	crystalline CH_3SO_3Na (Risberg et al., experimental data, ref 28)[a]	CH_3SO_3Na particles at 80% RH (this work)	$CH_3SO_3^-$ ions in water (Risberg et al., DFT calculated data, ref 28)	assignment (Risberg et al., ref 28)[b]
1044	1050			
1052	1060			
1062	**1069**	1049	998	A_1, ν_3, SO_3 sym stretch
1076	1076			
1197	**1201**	1192	1161	E, ν_8, SO_3 asym stretch
1209	1214			
1248	1250			
1331	1337	1331	1332	A_1, ν_2, CH_3 sym def

[a] Solid-state effects cause splitting of fundamental normal modes. Frequencies marked in bold font indicate the most intensive IR mode. [b] Detailed analysis of the vibrational spectra and assignment of the specific modes are described by Risberg et al. (ref 28).

TABLE 2: Polynomial Coefficients Obtained from Curve Fitting of the WSR data as a Function of Water Activity (a_w) for Solutes Used in This Work[a]

	a_0	a_1	a_2	a_3	a_4	a_5	valid a_w range
CH_3SO_3Na	−0.00739	5.25604	−29.1792	100.410	−108.406	55.4494	0.5−0.8
$CH_3SO_3NH_4$	−0.07217	8.88384	0.093120	22.8091	−11.1382	13.0063	0−0.8
$(CH_3SO_3)_2Mg$	1.96984	−3.68323	126.548	−343.562	389.054	−145.614	0−0.8
$(CH_3SO_3)_2Ca$	−0.006202	15.7069	−117.932	400.765	−507.818	249.810	0−0.8

[a] $WSR = a_0 + a_1a_w + a_2a_w^2 + a_3a_w^3 + a_4a_w^4 + a_5a_w^5$.

polynomial fitting of the WSR data with equal weights as a function of RH was applied, and the corresponding polynomial coefficients are tabulated in Table 2 for all four $(CH_3SO_3)_nX$ salts studied in this work. The dashed line in Figure 3c shows the WSR ratios of CH_3SO_3Na particles inferred from the levitation study of Peng and Chan.[20] The vertical arrows indicate DRH and ERH values reported in the same study. As seen, the hydration/dehydration cycle of CH_3SO_3Na particles recorded in our micro-FTIR experiment agrees well with the previously published data.[20] We note that some of the most recent hydration studies[34,35] of substrate-deposited particles have reported on previously unrecognized solid-to-solid phase transition and deliquescence delay effects, which were believed to be induced by surface adsorbed water in experiments employing prolonged exposure of particles to water vapor. However, these effects were not evident in the hydration/dehydration cycle of CH_3SO_3Na particles presented here.

Figure 5a shows IR spectra of $CH_3SO_3NH_4$ particles in a hydration experiment. At 0% RH, the IR spectrum has strong and broad $\nu_8(-SO_3^-)$ and $\nu_3(-SO_3^-)$ bands near 1189 and 1049 cm^{-1}, respectively. Structured doublets near 3200 and 3050 cm^{-1} and a peak near 1435 cm^{-1} are assigned to $\nu_3(NH_4^+)$ stretch and $\nu_4(NH_4^+)$ bending modes, respectively.[36] The broader band shape and peak positions close to those observed for deliquesced CH_3SO_3Na particles may suggest that $CH_3SO_3NH_4$ particles exist in a chemical environment similar to droplet, even at 0% RH. Condensed-phase water starts to appear at very low RH and is continuously taken up over the course of hydration. At high RH, e.g., 80% RH, no apparent broadening and red shifts are observed for the $-SO_3^-$ and the NH_4^+ absorption bands. The integrated absorbance of the $\nu_3(NH_4^+)$ band at 2550−3400 cm^{-1} measured at 0% RH was used to subtract the NH_4^+ contribution from the overlapping water bands. Figure 5b shows the variation of WSRs for $CH_3SO_3NH_4$ particles over the course of hydration and dehydration experiment. Polynomial coefficients resulted from the curve fitting of the WSR data as a function of RH are tabulated in Table 2.

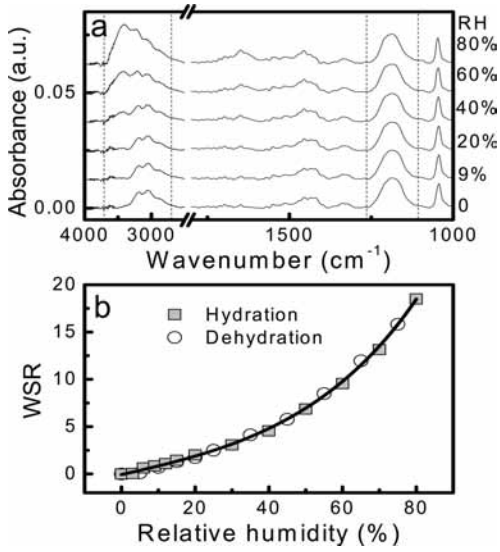

Figure 5. (a) IR spectra of $CH_3SO_3NH_4$ particles undergoing hydration. Spectra are vertically offset for clarity. (b) Variation in WSRs in $CH_3SO_3NH_4$ particles during hydration and dehydration experiments. Solid line is a polynomial fit (Table 2).

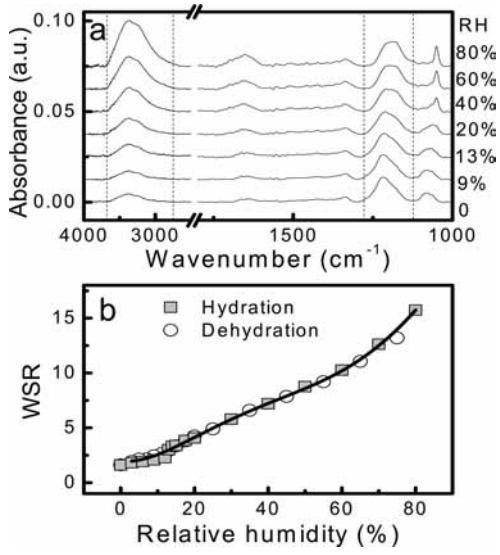

Figure 6. (a) IR spectra of $(CH_3SO_3)_2Mg$ particles undergoing hydration. Spectra are vertically offset for clarity. (b) Water-to-solute ratios (WSR) in $(CH_3SO_3)_2Mg$ particles during a single-cycle hydration/dehydration experiment. Solid line is a polynomial fit (Table 2).

Figures 6 and 7 show IR spectra and characteristic WSR variations in hydration/dehydration experiments with $(CH_3SO_3)_2Mg$ and $(CH_3SO_3)_2Ca$ particles, respectively. Unlike $(CH_3SO_3)_2Ca$, the IR spectrum of $(CH_3SO_3)_2Mg$ particles reveals substantial condensed-phase water absorption even at 0% RH. Also, relatively broad absorption bands near 1220 and 1080 cm^{-1} due to $\nu_8(-SO_3^-)$and $\nu_3(-SO_3^-)$ are observed for both samples. Similarly to the $CH_3SO_3NH_4$ particles, during the hydration, $(CH_3SO_3)_2Mg$ and $(CH_3SO_3)_2Ca$ particles absorb and evaporate water continuously and reversibly as the RH increases and decreases. No hysteresis between hydration and dehydration experiments is observed. In the hydration experiments red shifts of both $\nu_8(-SO_3^-)$and $\nu_3(-SO_3^-)$ bands are observed. Furthermore, the variations of WSRs are quantitatively similar for $(CH_3SO_3)_2Mg$ and $(CH_3SO_3)_2Ca$ particles and their corresponding polynomial fitting coefficients are also tabulated in Table 2.

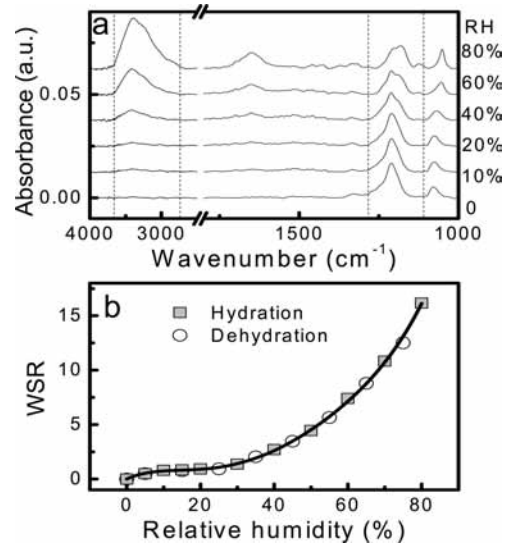

Figure 7. (a) IR spectra of $(CH_3SO_3)_2Ca$ particles undergoing hydration. Spectra are vertically offset for clarity. (b) Variations in WSRs in $(CH_3SO_3)_2Ca$ particles during hydration and dehydration experiments. Solid line is a polynomial fit (Table 2).

Conclusion and Atmospheric Implications

Comparison of the WSR data presented above with the corresponding literature values reported for common sea salt compounds is included in the Supporting Information (supplement A). The WSR values measured for CH_3SO_3Na, $CH_3SO_3NH_4$, and $(CH_3SO_3)_2Mg$ particles appear to be approximately in the same range as those reported for NaCl and $MgCl_2$—two major components of sea salt. Therefore, atmospheric processing of sea salt particles with methanesulfonic acid likely would not impact drastically their hygroscopic properties.

In contrast, atmospheric processing of mineral dust carbonates with methanesulfonic acid according to the reaction

$$CaCO_3(s) + CH_3SO_3H(aq/g) \rightarrow (CH_3SO_3)_2Ca(aq) + CO_2(g) + H_2O \quad (R2)$$

may have a substantial impact on physicochemical properties of mineral dust particles transported over the marine boundary layer of oceans. Similar to the $CaCO_3$(s)-to-Ca(NO_3)(aq) heterogeneous chemistry,[8,9,37] highly hygroscopic $(CH_3SO_3)_2$Ca(aq) and $(CH_3SO_3)_2$Mg(aq) products can be formed on the surface of crystalline calcite ($CaCO_3$) and dolomite (CaMg$(CO_3)_2$) particles, converting those nonsoluble particles into substantially hygroscopic as the reaction proceeds. In principle, the conversion can occur through both heterogeneous gas-to-particle reaction and cloud processing of particles (aqueous−solid-phase reaction inside cloud microdroplets). However, the gas-to-particle reaction of CH_3SO_3H is fairly slow because of its low vapor pressure. In turn, aqueous−solid heterogeneous reactions of highly soluble and mobile CH_3SO_3H may exhibit fast kinetics and complete reaction extent.

To illustrate relative importance of gas-to-particle and aqueous−solid heterogeneous reaction mechanisms, we performed series of tests where $CaCO_3$ particles have been exposed to gas-phase and aqueous-phase CH_3SO_3H reactant. Details of these experiments are included in the Supporting Information (supplement B). Figure 8 shows SEM images of $CaCO_3$ particles prior and after the exposures in three different tests: (A1 → A2)—exposure to 2×10^{-4} Torr (saturated vapor pressure of gaseous CH_3SO_3H at 22 °C) and 40% RH for 12 h at

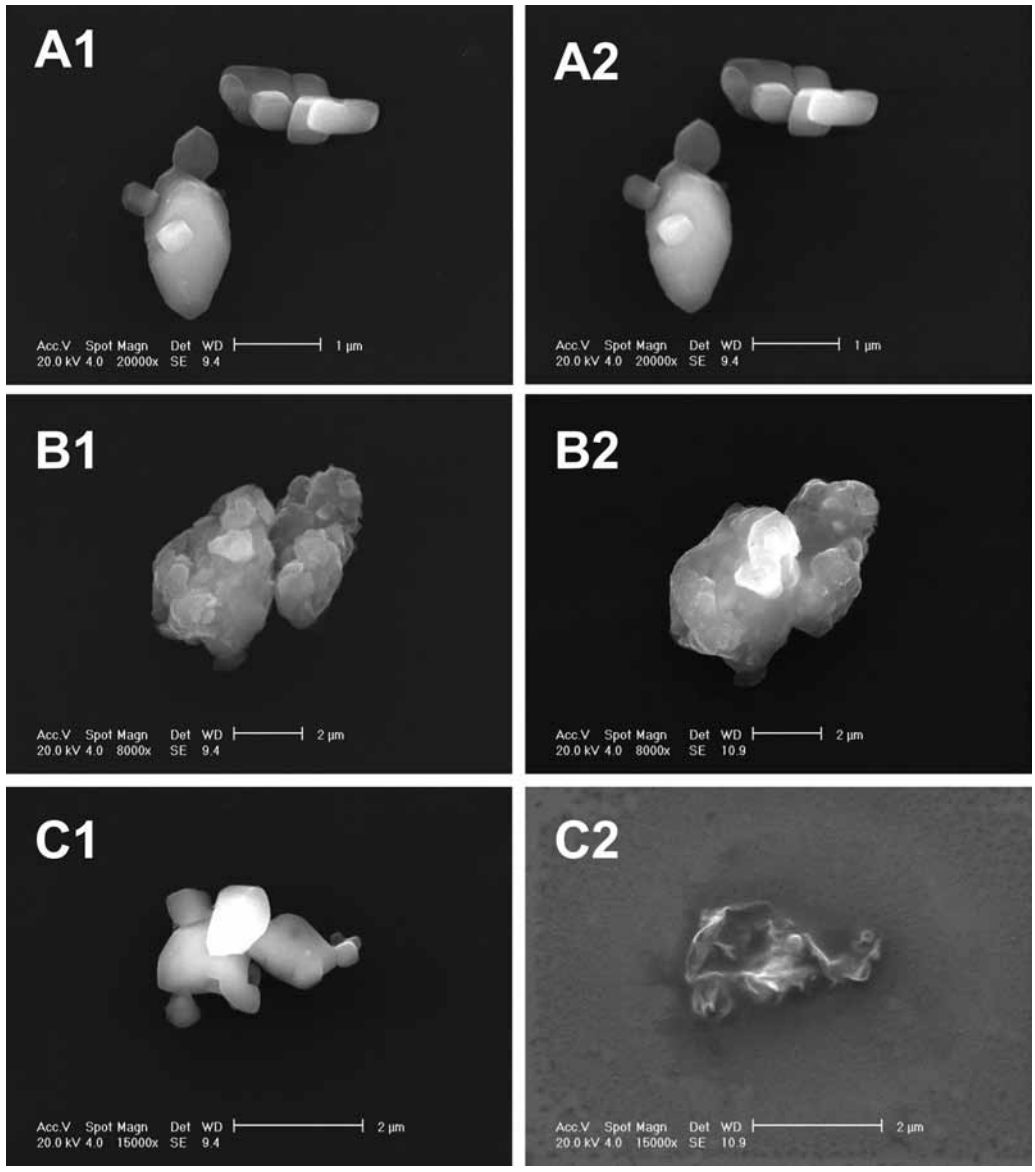

Figure 8. SEM images of $CaCO_3$ particles before (left panels) and after (right panels) reaction with CH_3SO_3H in three different experiments: (A1 → A2)—exposure to 2×10^{-4} Torr of gaseous CH_3SO_3H and 40% RH for 12 h, (B1 → B2) and (C1 → C2)—2 min of exposure to aqueous solution of CH_3SO_3H at 3×10^{-3} and 3×10^{-2} M concentrations, respectively.

atmospheric pressure; (B1 → B2) and (C1 → C2)—1 min of exposure to aqueous solutions of CH_3SO_3H at 3×10^{-3} and 3×10^{-2} M concentrations, respectively. In the gas-to-particle reaction test, no change in particle morphology is observed even after prolonged (12 h) exposure to the saturated vapor of CH_3SO_3H. In contrast, substantial changes in particle morphology indicative of reactive transformation are evident after nearly immediate (~2 min) exposures to diluted solutions of CH_3SO_3H in the aqueous−solid reaction tests. We note that concentration of 3×10^{-2} M used in test C corresponds to an equivalent of saturated gas-phase CH_3SO_3H fully dissolved in microdroplets of an atmospheric cloud with characteristic liquid water content (LWC) of 0.4 g/m^3, which is typical for MBL. Concentration in test B is therefore by a factor of 10 lower than that.

The conclusion from this set of experiments is that the aqueous−solid mechanism of reaction R2 is more efficient than the gas-to-particle processes in possible atmospheric transformation of $CaCO_3$ particles to $(CH_3SO_3)_2Ca$. Consecutively, this transformation can impact heterogeneous chemistry of mineral dust particles and modify their optical properties and abilities to serve as cloud condensation and ice nuclei. These effects may have important atmospheric environment implications in terms of the continuing reactivity of mineral dust and its direct and indirect effects on radiative forcing of climate.

Acknowledgment. The work was supported by the Radiation Science program at the National Aeronautics and Space Administration (Grant No. NNG06GE89G) and the Atmospheric Science Program of the Department of Energy's Office of Biological and Environmental Research (DOE OBER). The research was performed in the Environmental Molecular Sciences Laboratory (EMSL), a national scientific user facility sponsored by the Department of Energy's Office of Biological and Environmental Research (DOE OBER) and located at Pacific Northwest National Laboratory (PNNL). PNNL is operated for the U.S. Department of Energy by Battelle Memorial Institute under contract no. DE-AC05-76RL01830.

Supporting Information Available: Variations of WSRs in particles composed of single salts relevant to marine aerosol (supplement A) and test exposures of substrate-deposited CaCO3 particles to gas-phase and aqueous-phase CH_3SO_3H reactant

(supplement B). This material is available free of charge via the Internet at http://pubs.acs.org.

References and Notes

(1) Andreae, M. O.; Crutzen, P. J. *Science* **1997**, *276*, 1052.
(2) Baker, M. B. *Science* **1997**, *276*, 1072.
(3) Ravishankara, A. R. *Science* **1997**, *276*, 1058.
(4) Seinfeld, J. H.; Pandis, S. N. *Atmospheric Chemistry and Physiscs: from Air Polution to climate Change*; Wiley and Sons, Inc.: New York, 1998.
(5) Finlayson-Pitts, B. J.; Pitts, J. N. J. *Chemistry of the Upper and Lower Atmosphere—Theory, Experiments, and Applications*; Academic Press: San Diego, CA, 2000.
(6) Liu, Y.; Cain, J. P.; Wang, H.; Laskin, A. *J. Phys. Chem. A* **2007**, *111*, 10026.
(7) Saul, T. D.; Tolocka, M. P.; Johnston, M. V. *J. Phys. Chem. A* **2006**, *110*, 7614.
(8) Liu, Y.; Gibson, E. R.; Cain, J. P.; Wang, H.; Grassian, V. H.; Laskin, A. *J. Phys. Chem. A* **2008**, *112*, 1561.
(9) Krueger, B. J.; Grassian, V. H.; Laskin, A.; Cowin, J. P. *Geophys. Res. Lett.* **2003**, *30*, 1148.
(10) Tang, I. N.; Wong, W. T.; Munkelwitz, H. R. *Atmos. Environ.* **1981**, *15*, 2463.
(11) Tang, I. N. *J. Geophys. Res., [Atmos.]* **1997**, *102*, 1883.
(12) Martin, S. T. *Chem. Rev.* **2000**, *100*, 3403.
(13) Kelly, J. T.; Wexler, A. S. *J. Geophys. Res., [Atmos.]* **2005**, *110*, D11201.
(14) Kelly, J. T.; Chuang, C. C.; Wexler, A. S. *Atmos. Environ.* **2007**, *41*, 2904.
(15) Gibson, E. R.; Hudson, P. K.; Grassian, V. H. *J. Phys. Chem. A* **2006**, *110*, 11783.
(16) Andreae, M. O. *Mar. Chem.* **1990**, *30*, 1.
(17) Charlson, R. J.; Lovelock, J. E.; Andreae, M. O.; Warren, S. G. *Nature* **1987**, *326*, 655.
(18) von Glasow, R.; Crutzen, P. J. *Atmos. Chem. Phys.* **2004**, *4*, 589.
(19) Hopkins, R. J.; Desyaterik, Y.; Tivanski, A. V.; Zaveri, R. A.; Berkowitz, C. M.; Tyliszczak, T.; Gilles, M. K.; Laskin, A. *J. Geophys. Res., [Atmos.]* **2008**, *113*, D04209.
(20) Peng, C. G.; Chan, C. K. *Atmos. Environ.* **2001**, *35*, 1183.
(21) Liu, Y.; Yang, Z.; Desyaterik, Y.; Gassman, P. L.; Wang, H.; Laskin, A. *Anal. Chem.* **2008**, *80*, 633.
(22) Laskin, A.; Wietsma, T. W.; Krueger, B. J.; Grassian, V. H. *J. Geophy. Res., [Atmos.]* **2005**, *110*, D10208.
(23) Socrates, G. *Infrared and Raman Characteristic Group Frequencies: Tables and Charts*, 3rd ed.; John Wiley & Sons: New York, 2001.
(24) Downing, H. D.; Williams, D. *J. Geophys. Res.* **1975**, *80*, 1656.
(25) Al-Abadleh, H. A.; Grassian, V. H. *J. Phys. Chem. B* **2003**, *107*, 10829.
(26) Sporleder, D.; Ewing, G. E. *J. Phys. Chem. A* **2001**, *105*, 1838.
(27) Al-Abadleh, H. A.; Grassian, V. H. *Langmuir* **2003**, *19*, 341.
(28) Risberg, E. D.; Eriksson, L.; Mink, J.; Pettersson, L. G. M.; Skripkin, M. Y.; Sandstrom, M. *Inorg. Chem.* **2007**, *46*, 8332.
(29) Zhao, L. J.; Zhang, Y. H.; Wei, Z. F.; Cheng, H.; Li, X. H. *J. Phys. Chem. A* **2006**, *110*, 951.
(30) Frost, R. L.; James, D. W. *J. Chem. Soc., Faraday Trans. 1* **1982**, *78*, 3249.
(31) Frost, R. L.; James, D. W. *J. Chem. Soc., Faraday Trans. 1* **1982**, *78*, 3223.
(32) Vollmar, P. M. *J. Chem. Phys.* **1963**, *39*, 2236.
(33) Weis, D. D.; Ewing, G. E. *J. Phys. Chem. A* **1999**, *103*, 4865.
(34) Lu, P. D.; He, T.; Zhang, Y. H. *Geophys. Res. Lett.* **2008**, *35*, L20812.
(35) Lu, P. D.; Wang, F.; Zhao, L. J.; Li, W. X.; Li, X. H.; Dong, J. L.; Zhang, Y. H.; Lu, G. Q. *J. Chem. Phys.* **2008**, *129*, 8.
(36) Cziczo, D. J.; Abbatt, J. P. D. *J. Geophys. Res., [Atmos.]* **1999**, *104*, 13781.
(37) Laskin, A.; Iedema, M. J.; Ichkovich, A.; Graber, E. R.; Taraniuk, I.; Rudich, Y. *Faraday Discuss.* **2005**, *130*, 453.

JP8079149